



The OSMOND Detector - A Computer Model

JE Bateman, DM Duxbury

January 2014

©2014 Science and Technology Facilities Council



This work is licensed under a [Creative Commons Attribution 3.0 Unported License](https://creativecommons.org/licenses/by/3.0/).

Enquiries concerning this report should be addressed to:

RAL Library
STFC Rutherford Appleton Laboratory
Harwell Oxford
Didcot
OX11 0QX

Tel: +44(0)1235 445384
Fax: +44(0)1235 446403
email: libraryral@stfc.ac.uk

Science and Technology Facilities Council reports are available online at: <http://epubs.stfc.ac.uk>

ISSN 1358-6254

Neither the Council nor the Laboratory accept any responsibility for loss or damage arising from the use of information contained in any of their reports or in any communication about their tests or investigations.

THE OSMOND DETECTOR – A COMPUTER MODEL

J.E.Bateman, D.M.Duxbury

Technology Dept., Science and Technology Facilities Council, Rutherford Appleton Laboratory,
Harwell Oxford, Didcot, Oxfordshire, OX11 0QX, U.K.

13 January 2014

Abstract

A computer model of the Off Specular MicroStrip Neutron Detector (OSMOND) is described. The model is used to aid the analysis of the experimental results from the detector and examine possible avenues for improved performance.

1. Introduction

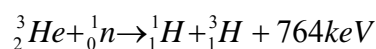
The OSMOND (Off Specular MicRostrip Neutron Detector) detector is an MSGC-based 1-D position sensitive device with a pitch of 0.5mm operating in a pressurised gas mixture of ^3He (3.6 bar) and CF_4 (4.0 bar). The detector has anode strips (65 mm long) which are made to point at the sample position, whilst the neutron induced electron clouds are drifted across the aperture gap (50mm) perpendicularly to the direction of the incident neutron beam (collimated by narrow slits 50mm long). This ‘pointing anode’ geometry gives parallax free detection with spatial resolution of $\sim 0.7\text{mm}$ FWHM and is used successfully on the CRISP and POLREF neutron reflectometers on ISIS. The detailed design of the OSMOND detector and its overall performance is reported in ref. [1].

The principle of the detector is to exploit, for the benefit of neutron beam applications, the fast parallel data taking pioneered by the HOTWAXS detector [2] for x-ray scattering. This involves having independent amplification and discrimination on every active strip (640 in total) and capturing the data streams in parallel to realise the possibility of very high global data rates ($>100\text{MHz}$). The constraints of the ISIS Data Acquisition Environment (DAE) [3] dictated that a global readout system, the Ripple Priority Encoder (RPE) based on priority encoding of the channel number be implemented, thus limiting the data capture rate to $\sim 1\text{MHz}$. This data capture rate is a considerable improvement on that available from the pre-existing scintillation counter [1].

The design study for OSMOND was based on an earlier computer model of the detection process of neutrons in the gas of the detector [4]. In view of the well-established high rate capabilities of the MSGC (the discussion in ref. [1] shows that the neutron beams cannot challenge the detector in this respect) the computer model is restricted to addressing the important questions of spatial resolution and detection efficiency. The basic model of ref. [4] has been developed and extended to make it more flexible to permit detailed comparison with the experimental results from the beam-line commissioning of the detector. The rapid success of the detector and the pressure to release the instrument to the user community restricted the desirable diagnostic phase of operation on installation. The new model has been adapted to help analyse the limited data collected and permit assessment of some of the unknown detector parameters.

2. The Model

The detection process for slow neutrons uses the reaction:



which results in the emission of a 0.191MeV triton and a collinear 0.573MeV proton, emitted back to back. The orientation of the track pair is random (i.e. isotropic). Thus in the gas mixture, the helium density and pressure determine the neutron stopping power (and thus the *conversion efficiency*), and the density and pressure of the CF_4

quencher gas (to first order) determines the range of the particles (and thus the spatial resolution). The latter fact follows because the density of CF_4 at NTP is 30 times that of ^3He . As will be shown below the quencher pressure also impacts on the trigger efficiency and hence on the overall detection efficiency.

These interactions take place in a gas-filled box, 65mm deep (x-coordinate along the strip length) by 50mm (y-coordinate in the drift direction) by 330mm (z-coordinate perpendicular to the strips – the “readout” direction). The very slight taper on the strips (0.483mm at the input face to 0.5mm at the far end) is ignored in the model. The beam is assumed to enter parallel to the anode strips (parallel to the x-axis) and to be uniformly distributed across the drift gap (y-direction). Thus the x-dimension determines the stopping efficiency in the usual way but does not enter into the detection model otherwise (provided the beam is accurately aligned). The distribution of the input beam in the z-direction is determined by the collimation assumed for the model. The y-coordinate of any event determines the magnitude of the diffusion spreading experienced by the secondary electrons (released by the primary particles) in their transit to the amplifying strip anode and so affects the spatial resolution directly.

Each event releases 0.764MeV of energy in the gas which results in $\sim 1.4 \times 10^4$ secondary electrons (as $>90\%$ of the particle energy is deposited in the CF_4 component the mean energy per ion pair (W_{ip}) in this gas mixture is taken as that of CF_4 – 54eV [5]). These electrons are released to move to the nearest anode under the influence of the drift field ($\sim 4\text{kV/cm}$ in the actual detector). These electrons are initially distributed along the particle tracks proportionately to the specific energy loss curve (Bragg curve) for each particle and spread out laterally as they drift according to the standard diffusion model. The data used for particle range and specific energy loss is taken from reference [6]. The standard deviation of a punctual cloud arriving at the anode is given by $\sigma_0 \sqrt{y}$ where σ_0 is usually quoted in $\mu\text{m/cm}^{1/2}$. For a given gas mixture σ_0 is a function of the drift field and the gas pressure. As no data is found in the literature for the parameters in OSMOND a typical value of $150\mu\text{m/cm}^{1/2}$ is adopted initially. The diffusion process is completely specified by this parameter and details of the drift field are irrelevant, the field being assumed uniform and parallel.

On arrival at an anode strip each electron is amplified (on average) by a factor of ~ 10 and the total charge on each anode is collected, amplified and presented to a discriminator. If this discriminator threshold (LLD) is exceeded the digital readout is triggered and the event is registered to the appropriate channel in the data capture system. In general more than one anode channel will trigger and the fraction of events in which at least one trigger is recorded is called the *readout efficiency*. The overall detector efficiency is the product of the conversion efficiency and the readout efficiency with a correction added for the significant window losses of the actual detector.

The decision at each discriminator is made on the (charge) pulse height of the strip amplifier which has a fraction of the $\sim 1.4 \times 10^5$ electrons available from the event. This signal is subject to amplifier noise and avalanche noise which broaden the ideal (narrow peak) pulse height distribution very significantly. Since every event delivers the same (average) energy and charge it is convenient to measure the pulse height in terms of energy deposit and the LLD in terms of the fraction of the total deposit

(0.764MeV) it represents. Thus the gain of the anodes does not enter explicitly but is reflected in the electronic and avalanche noise parameters which are functions of the anode gain. The standard deviations of these dispersing processes (assumed to be normal distributions) are σ_{en} and σ_{av} . The values used in the model are estimated from the experimental data to be $\sigma_{en} = 4200$ electrons = 22.7keV = 0.03 (LLD) and $\sigma_{av} = 0.025/\sqrt{E_s}$ where E_s is the energy deposit in the strip in MeV. The electronic noise is additive but the avalanche noise is specified (and applied) as a multiplicative error as it is a statistical effect of the gas amplification.

Two types of readout are available for the detector. In the original multi-channel data capture system of the HOTWAXS detector (designated HWR – HOTWAXS Readout) all triggers from an event are stored in a bank of scalers. Since this is true parallel readout the maximum data capture rates are greater than 1MHz / channel and hundreds of MHz globally. The only demerit of this readout is the loss of numerical exactitude in the event count as the events with multiple triggers lead to a small amount of double counting. Under the usual operating conditions the count rate is exaggerated by a factor of ~ 1.5 . This factor is constant for a given LLD setting and causes no distortion of any position spectrum. The readout used in OSMOND, a Ripple Priority Encoder (RPE), is a global readout which delivers only one channel address per event – the centre channel of a three hit event, the lowest channel of a two hit event and the channel itself for a single hit. Being global this limits the detector to a rate of just over 1MHz but matches the detector to the limitations of the ISIS DAE system and delivers a small amount of centroiding. The model shows that the RPE systematically delivers marginally better spatial resolution than the HWR. The data capture aspects are easily represented in the model.

2.1 Some Operational Details

Incident Beam Definition – An arbitrary array of strip bins is set up (large enough to accommodate any proposed beam) and the origin of the axis system taken at the centre of the central strip. Only the z-dimension (the detector measurement direction) is tracked explicitly. The y-dimension of the event is chosen randomly across the detector aperture and the x-dimension ignored on an event by event basis, the conversion efficiency simply being calculated by the usual absorption formula. The starting (incident) z-position is defined by the user according to requirements, the simplest being $z = 0.0$ or an infinitely narrow beam applied to the centre of the central strip.

Event Definition – Since the device is sensitive only in the z-direction an isotropic event orientation is simply achieved by taking a random cosine for the angle between the tracks and the z-axis. The proton and triton are randomly assigned to the right or left on the z-axis (projection).

Electron Number Definition – For each track, ideally the number of electrons tracked is the (particle energy) / W_{ip} . However, because of the dominant effect of the electronic and avalanche noise this is unnecessarily laborious as the electron statistics only require to be good enough to avoid broadening the pulse height spectrum. Monitoring the spectrum of total energy deposits in the model shows that the electron statistics can be reduced by up to a factor of 500 without showing any effect. This

dramatically reduces run times and is easily arranged by multiplying the value assumed for W_{ip} by the appropriate factor.

Bragg Curve Definition – The particle ranges and specific energy loss ($dE/dx(E)$) curves from ref [6] are configured in units of g/cm^2 so that variable gas pressures may be accommodated. The $dE/dx(E)$ curves from [6] are transformed into $dE/dx(x)$ (i.e. Bragg) curves. The data for air [5] is used for CF_4 and the mass-range values scaled by the factor $(Z_N/Z_C)^{0.52}$ where Z (the atomic number) is 7 for air (nitrogen – N) and taken as 9 for CF_4 . The appropriate number of secondary electrons (as defined above) is distributed along the Bragg curve of each particle using the usual MonteCarlo weighting technique. The displacement of each electron is projected onto the z-axis using the randomly generated cosine to give the shift relative to the incident neutron position.

Diffusion Definition – The position of the event in the y-dimension (detector aperture) is generated randomly for each event and the appropriate random normal dispersion error ($\sigma_0\sqrt{y}$) applied to the z-component of each electron calculated above.

Strip Energy Definition – Now the final z-coordinate of each electron arriving at the MSGC plane is to hand. The electrons of a given event are histogrammed into the bin array set up at the beginning with W_{ip} being added to a bin for each electron captured in it. Thus on completion of the full number of electrons in the event each bin contains the energy deposited in that strip (in MeV). In order to generate a realistic pulse height the energy value in each strip bin is dispersed with the electronic noise σ_{en} and the avalanche noise σ_{av} specified above.

Hit Definition and Digital Readout – The pulse heights in the strip energy array are now tested against the LLD setting. The index of any successful bin (pulse height > LLD) is then used to increment the HWR digital array. The address of the single channel output for the RPE array is generated by interrogating the bin energy array from either end and applying the algorithm described above. Digital events are thus accumulated in two separate arrays while the strip energy array is cleared for the next event.

Pulse Height Spectra – The total pulse height (energy) deposited (in all bins activated) is histogrammed in a pulse height spectrum and a similar spectrum of the pulse heights in the central strip bin is also stored.

Data Output – the two position arrays and the two pulse height spectra are saved to disk with a text file containing the calculated efficiencies and spatial resolutions (FWHM) pertaining to the two readout modes (HWR and RPE) and all the variable parameters of that particular run. Figure 1 shows the recorded hit patterns from which the FWHM is calculated using the standard statistical algorithm. The output text file is also displayed. A low value of LLD (= 0.3) is chosen for this example to highlight the differences between the HWR and the RPE readouts, namely the larger FWHM of the HWR, the over-counting of the HWR (x1.62) and the low bias on the RPE distribution due to the truncating algorithm used in it.

Figure 2 shows the simulated pulse height spectrum from strip zero (the zero-width beam is located in the middle of this strip) along with the spectrum of the

summed pulse heights generated by any event. As expected this distribution is centred on the total energy deposit (764keV) and represents the “energy resolution” of the simulated counter. This spectrum is matched to the experimentally observed pulse height resolution to take account of the counter gain, electronic noise and avalanche noise.

The program is written in Decimal BASIC. A typical run uses 50 000 event starts and takes approximately 5 minutes to complete.

3. Pulse Height Studies

Each neutron interaction in the detector releases precisely 764keV of energy leading to a charge deposit of $\sim 1.4 \times 10^4$ electrons with a FWHM variation of 2.0%. This distribution is broadened by avalanche statistical noise and amplifier noise to yield a peak typified by the total energy pulse height spectrum of Figure 2. While this advantageous pulse height distribution is not made use of in normal operation it is useful for calibration purposes, and when compared with the simulated spectra for the elucidation of otherwise unknown parameters. A clean peak such as this can only arise if the sensitive detector volume is large enough to completely contain all pt (proton-triton) tracks. In a single strip this is clearly far from the case so in commissioning tests the effective strip width was raised by successively bussing adjacent strips into one charge amplifier until a satisfactory peak appeared. Figure 3 shows the PH (pulse height) spectra obtained from (successively) 1, 2, 3 and 4 channels summed while the detector was uniformly irradiated in the test facility (a moderated Am-Be neutron source). In Figure 3 the full energy peak becomes just visible from the 2 strip sum upwards and the peak position in the 4 strip sum spectrum was used to calibrate the LLD settings as a fraction of the total energy deposit.

The computer model was adjusted to simulate the PH spectra of Figure 3 by simply increasing the strip width *pro rata*. The simulation was “irradiated” uniformly over 5 strips to generate the leakage into the target strip (number zero) from adjacent strips and so match the experimental situation. Figure 4 shows the simulated PH spectra which are seen to match the shapes of the experimental spectra closely. (The relative vertical normalisation between the curves is not accurately modelled in the 1 strip case because of the different irradiation geometry). When the experimental and simulated spectra are peak normalised for height and the “gains” adjusted to match the peak centroids, the distributions of Figures 3 and 4 match very well. Figure 5 illustrates the match for the 4 strip case. The small differences are due to experimental realities in the practical case – namely the fact that the amplifier noise increases with the extra capacitive loading of 4 strips leading to a slightly larger FWHM in the experimental spectrum and also the fact that noise is not inserted into empty channels in the simulation so that there is no “noise floor” for the amplifier noise in the simulated spectrum.

A distinct feature of the spectra in Figure 3 is the way in which the full energy peak drifts downwards as the number of summed strips increases (in contradistinction to the simulated ones of Figure 4 in which the peak drifts slightly upward). This is due to the loss of signal caused by capacitive charge sharing between the capacitance of the strips (C_s) and the preamplifier input capacitance (C_a). As the former increases the fraction of charge collected by the amplifier decreases as

$C_a/(C_a+C_s)$. Since the strips are all identical this becomes: $C_a/(C_a+nC)$ where n is the number of strips summed and C is the capacitance of a single strip. The gain normalisation factors required to bring each pair of spectra into agreement clearly represent this loss factor (the simulated spectra represent the full signal always). Figure 6 shows the result of fitting the inverses of the gain factors to the relation $1/(1+nC/C_a)$ (omitting $n=1$ as there is no discernable peak). The strip capacitance is found to be 4% of the amplifier input capacitance. Using this finding to adjust the experimental PH spectra leads to the corrected spectra of Figure 7. Using the values of the fitted function (in Figure 6) for $n=1$ and $n=4$ we can now correct for the slight error in the LLD calibration i.e. the true fraction of the total energy is 0.9 times that assigned by the simple calibration.

In the design modelling for OSMOND the major unknown was the electron diffusion constant (σ_0) – defined as the standard deviation of the lateral diffusion of a punctual electron deposit as it drifts through 1cm of gas in a given electric field (E) and at a given pressure (P). The usual units are microns/ $\sqrt{\text{cm}}$. There is no published data on this parameter relevant to the detector conditions so the simulations included a plausible range of values. Experimental data on other quenching gases such as CO_2 [7] shows that σ_0 typically shows a minimum as the electric field is increased. The value of E at the minimum rises with pressure ($\sim P^{1/2}$ in the case of CO_2 [7]) and σ_0 rises quite rapidly with E above the minimum. Thus the dependence of σ_0 for CF_4 on P and E can be in either sense depending on the position of our operating point relative to the minimum. In the course of the present simulation studies it transpired that the shape of the full energy peak in the PH spectrum in the 2 strip case is very sensitive to the value of σ_0 . Figure 8 shows the experimental 2-strip spectrum compared with simulations at $\sigma_0 = 50\mu\text{m}/\sqrt{\text{cm}}$, $100\mu\text{m}/\sqrt{\text{cm}}$ and $150\mu\text{m}/\sqrt{\text{cm}}$. Clearly a value of $100\mu\text{m}/\sqrt{\text{cm}}$ fits best and this value is used throughout the studies. This value is retained for higher gas pressures for lack of any better evidence.

4. Spatial Resolution Studies

In a 1-D position sensitive detector the spatial resolution is usually taken to be the FWHM of the response function of the system to an infinitely narrow slit beam – generally a normal (Gaussian) curve. In a simulation this is trivial to arrange but in the experimental case it is more complex depending on (in this case) generating by means of collimation, a neutron beam narrow enough to show the detector response. In the experimental case the FWHM is usually measured by fitting a Gaussian curve to the observed distribution. However this method becomes unreliable if too few data points are available as is the case when the FWHM decreases towards the strip width value, so for the simulations, the simple statistical method is applied. In this case the $\text{FWHM} = 2.36\sqrt{(\sigma^2 + 1/12)s_w}$ where σ^2 is the variance of the observed hit pattern about the mean and s_w is the strip width.

Because the spatial resolution dictated by the detection processes is roughly comparable to the strip width the spatial resolution is not totally invariant with respect to the impact point of a slit beam in the strip pattern. Thus a second mode of estimating the spatial resolution is adopted for some simulations – a broad beam (5 strips wide) is applied and the FWHM calculated from the difference in the variance of the observed distribution and that of the applied distribution (a 2.5mm wide top-

hat). Figure 9 shows the comparison between the two methods in a typical FWHM vs LLD plot under the standard running conditions. As one would expect the broad beam method generally gives a slightly larger FWHM. In practice the slit beam model is observed to agree best with the experimentally measured performance data.

Simulations were executed to reproduce the conditions of the detector during the commissioning tests so that a comparison could be made and the accuracy of the design predictions checked. A characteristic of this design is that the spatial resolution and the detection efficiency are both functions of the LLD parameter and that a certain degree of trade-off between these two vital parameters exists. Figure 10 shows the simulated FWHM as a function of the LLD setting evaluated using the slit beam method. The RPE readout system has a diagnostic mode which records the numbers of single, double and treble hits which go to make the typical distribution of Figure 1. Plotting the fraction of these cohorts as a function of LLD is a useful diagnostic to examine in conjunction with the FWHM plot of Figure 10. The simulated fractions are plotted along with the experimental results in Figure 11. In order to bring the curves into conjunction the LLD values of the experimental data has been multiplied by a factor of 0.83.

Without agreeing precisely the experimental FWHM in Figure 10 is close to the simulated curve when the LLD correction factor (evaluated in Section 3 above) of 0.9 is applied to the experimental data. The plot shows some characteristics of the two readout systems: the HWR FWHM rises quite sharply as the LLD reduces below 0.4 due to the increasing number of triggers possible from in-leakage of events from neighbouring strips while the RPE FWHM actually decreases in the same region. This is because the RPE algorithm effectively centroids the hit pattern of an event so that as triple hits replace double hits the variance decreases. Double hits cannot be centroided so that when they dominate the FWHM has a slight maximum. It is interesting to note that above $LLD \sim 0.4$ (a likely operating point) there is little difference between the two readout systems so that the spatial resolution will be preserved if the change to a high rate readout is made.

The correction factor of 0.83 applied in Figure 11 is slightly stronger than the estimated correction required for the LLD due to the calibration error (0.9) and the mechanism behind the discrepancy is not understood. However, the general concurrence of the three curves is reassuring.

5. Detection Efficiency Studies

The detection efficiency of OSMOND is a product of three factors: the detector window transmission factor (F_w), the neutron conversion factor (F_c) and the readout efficiency (F_r). The window factor $F_w = 0.782$ and varies little between $\lambda = 1\text{\AA}$ and $\lambda = 5\text{\AA}$. The conversion factor for $3.6 \times 6.5 \text{ bar-cm}$ of ^3He is $F_c = 0.85$ at $\lambda = 1\text{\AA}$, 0.97 at $\lambda = 2\text{\AA}$ and >0.99 for $\lambda > 3\text{\AA}$. The readout efficiency F_r is a function of the LLD setting and varies from ~ 1.0 to <0.1 as the LLD is raised from 0 to 0.9. Thus the maximum possible overall efficiencies $F_w F_c F_r$ are 66.5% (1\AA), 75.9% (2\AA) and 78.2% ($>3\text{\AA}$). (Above 5\AA the window factor begins to decline significantly). Figure 12 displays the overall detection efficiency predicted by the simulation for the standard

gas filling as a function of LLD. As is generally found with this type of detector, the detection efficiency (actually the readout efficiency F_r) starts to decline about the LLD setting at which the spatial resolution begins to improve and if a significant factor of improvement in the FWHM is desired then a correspondingly large loss of efficiency must be accepted. The simulation curve in Figure 12 is clearly just an integral above the LLD level of the single strip pulse height spectrum seen in Figure 2. Since the experimental version of the single strip PH spectrum (Figure 3) looks essentially similar (the low end leakage is not relevant as these events are detected in their “own” strip) one would expect the experimental version of the Figure 12 plot to be similar in shape. The very incompatible shape of the experimental data shown throws serious doubt on the value of the experimental data. A rerun of the experimental efficiency measurements is planned.

6. High Pressure Studies

As the OSMOND vessel is proofed to 14bar pressure it is useful to see what performance advantages are predicted by the model if the pressure of the gas components is increased. The above discussion (Section 5) shows that there is very little to be gained in terms of efficiency by increasing the ^3He partial pressure unless neutron wavelengths below 1\AA are important. The effect of increased CF_4 partial pressure on the spatial resolution and overall detection efficiency is examined in Figures 13, 14, 15. In these Figures the detector parameters are retained at exactly the same values as shown in Figure 1 with the exception of the partial pressure of CF_4 which is changed as indicated. These figures show that the computer model predicts that the FWHM decreases at all LLD settings as the pressure is raised while the detection efficiency in the region of $\text{LLD} > 0.3$ rises uniformly at all values of LLD. Combining these findings one can obtain a much reduced FWHM of 0.45mm at $\text{LLD}=0.54$ (RPE Readout) at 8bar CF_4 pressure while suffering only a small decline in detection efficiency from 0.663 to 0.573. The detection efficiency is the same for the HWR data and the FWHM shows a comparable decrease with the pressure increase (Figure 14). For these runs the diffusion parameter σ_0 was maintained at $100\mu\text{m}/\sqrt{\text{cm}}$. As noted in Section 3 above, σ_0 is dependent on pressure in a moderately complex way and so the effect of varying it on the FWHM in the 8bar simulation was checked. Figure 16 shows that at the LLD value of 0.54 chosen above the effect of a $\pm 50\mu\text{m}/\sqrt{\text{cm}}$ is a relatively minor effect and does not invalidate the improvement in spatial resolution predicted. In Figures 13 – 16 the broad beam measurement method is used.

7. Decreased Strip Width Studies

A much more expensive (though technically viable) potential method of improving the spatial resolution is to reduce the strip width of the MSGC pattern. Stable operation is quite feasible at a strip width of 0.25mm – half the present width. The model shows that in the standard OSMOND conditions changing this one parameter makes very little reduction in the FWHM and the CF_4 partial pressure must be raised to 8bar to achieve a useful reduction. Figure 17 shows the standard performance curve predicted under these conditions. At $\text{LLD}=0.3$ the RPE produces a FWHM of 0.38mm with a detection efficiency of 0.652 compared with the values of

0.45mm with 0.573 detection efficiency obtained in the case of the present 0.5mm strip width. On this basis the possibility of re-engineering the detector with narrower strips can be rejected as a viable improvement.

8. Conclusions

The computer model of the OSMOND detector created as an essential part of the design and proposal process [4] has been developed and extended to help with the assessment of the experimental performance of the device and to explore the options for further improvement. The ability of the new model to simulate the pulse height spectra anticipated in an individual channel has proved useful in correcting the discriminator calibration (in terms of the energy deposit of each event) and in estimating the major unknown in the experimental system, namely the electron diffusion constant.

Comparison of the model results with the measured spatial resolution shows that while very precise agreement is not obtained, the basic trends of the FWHM and the trigger multiplicities (as a function of the discriminator LLD) are well reproduced. On the other hand the experimental detection efficiency results do not agree with those from the model. As the latter are clearly a reflection of the single channel pulse height spectrum, the model version of which agrees well in shape with the experimental version, this throws doubt on the reliability of the experimental measurements which it is planned to repeat.

In addressing the potential of OSMOND for development the model shows that, as regards detection efficiency there is little to be gained by increasing the ^3He partial pressure (reducing the window loss is an improvement in hand) while as regards spatial resolution a significant reduction in the FWHM is possible by increasing the CF_4 partial pressure to 8bars. The model shows that the reduction of the MSGC strip width by a factor of two in a new design would provide only marginal improvement at great expense.

Acknowledgements

We wish to thank our colleagues N.J.Rhodes and E.M.Schooneveld of ISIS Department for their help and cooperation, in particular with the measurements shown in figure 3.

References

1. J.E.Bateman, R.Dalgliesh, D.M.Duxbury, W.I.Helsby, S.A.Holt, D.M^cPhail, A.S.Marsh, N.J.Rhodes, E.M.Schooneveld, E.J.Spill and R.Stephenson, Nucl. Instr. and Meth. **A698** (2012) 168
2. J.E.Bateman, G.E.Derbyshire, G.Diakun, D.M.Duxbury, J.P.A.Fairclough, I.Harvey, W.I.Helsby, J.D.Lipp, A.S.Marsh, J.Salisbury, G.Sankar, E.J.Spill, R.Stephenson and N.J.Terrill, Nucl. Instr. and Meth. **A580** (2007) 1526
3. M.W.Johnson, S.P.Quinton, SNS data acquisition electronics (DAE), RAL-NDRP-8504
4. J.E.Bateman, D.M.Duxbury, N.J.Rhodes, E.M.Schooneveld, and R.Stephenson, RAL-TR-2006-005
5. A. Scharma and R.Veenhof,
<http://consult.cern.ch/writeup/garfield/examples/gas/trans2000.html>.
6. J.F.Janni (1982) Atomic Data and Nuclear Data Tables, 27, Nos. 2-5 as reproduced in Kaye and Laby - Tables of Physical and Chemical Constants 16th Edition, Longman (1995).
7. Bobkov S. V., et. al. CERN-EP/83-81 (1983)

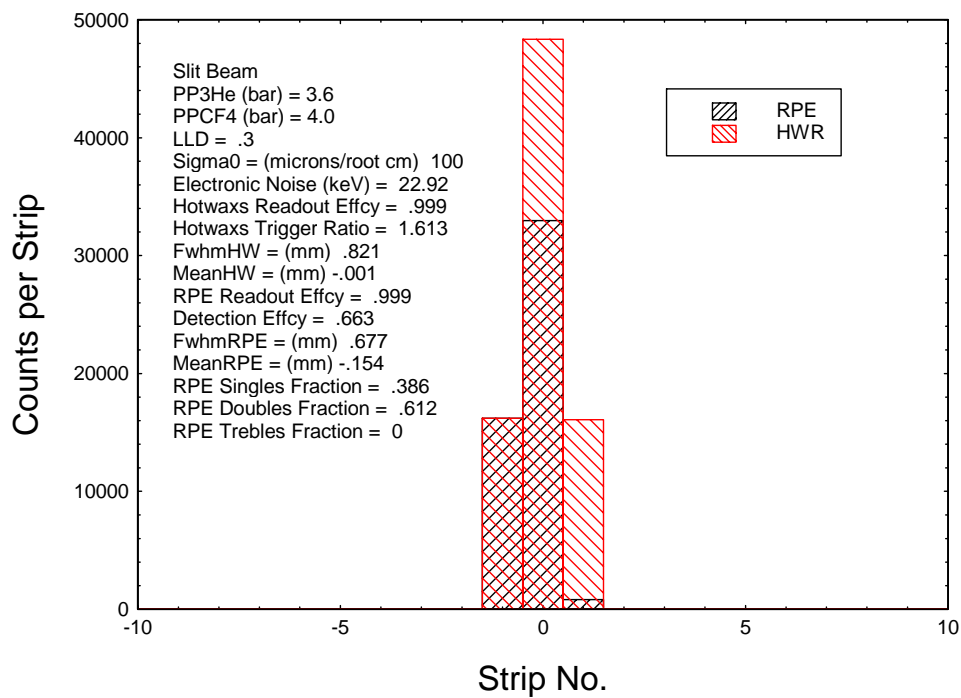


Figure 1: Typical simulated OSMOND Hit Patterns generated by the model.

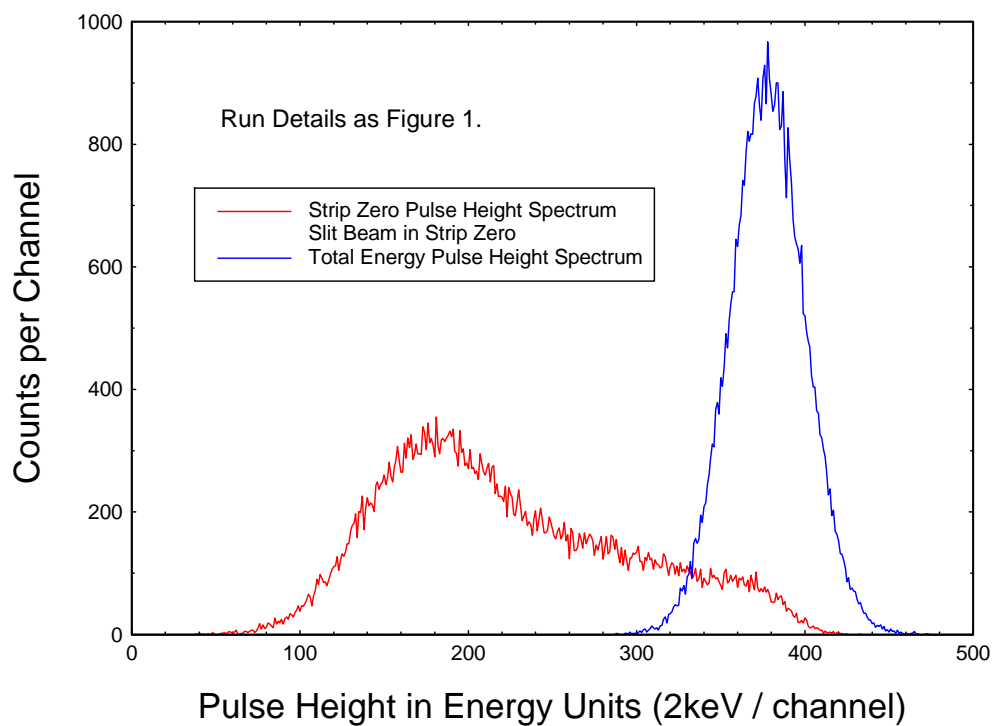


Figure 2: Simulated Total Energy and Central Strip Pulse Height Spectra.

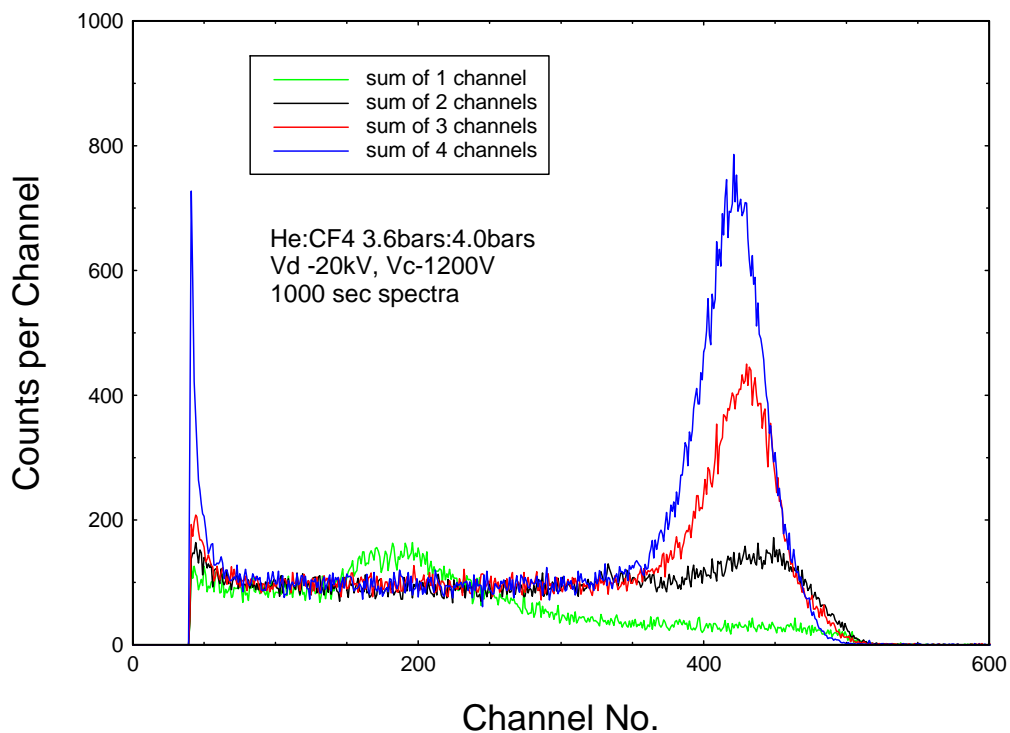


Figure 3: Experimental OSMOND Pulse Height Spectra from summed strips.

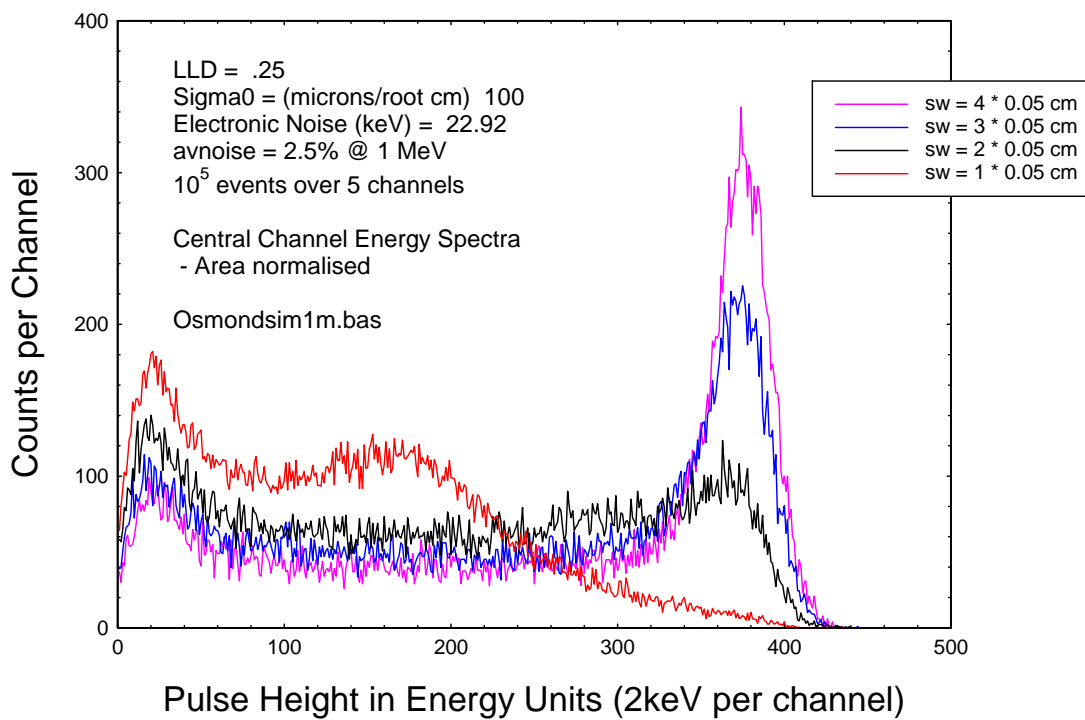


Figure 4: Simulated equivalent PH Spectra of the experimental sums.

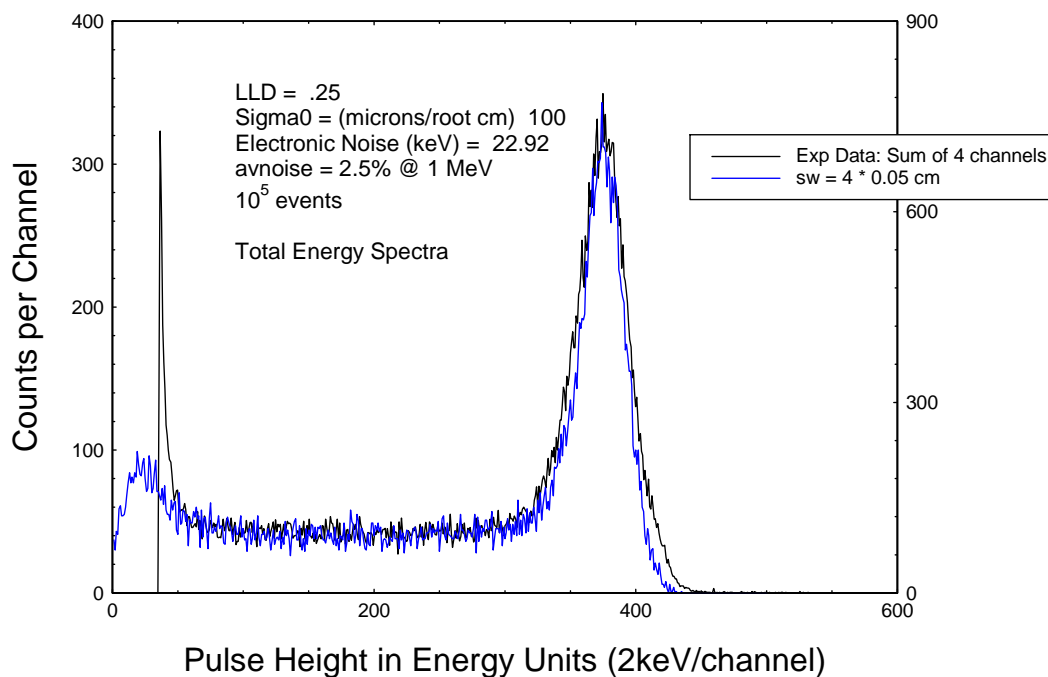


Figure 5: Comparison of Experimental and Simulated 4-strip PH Spectra.

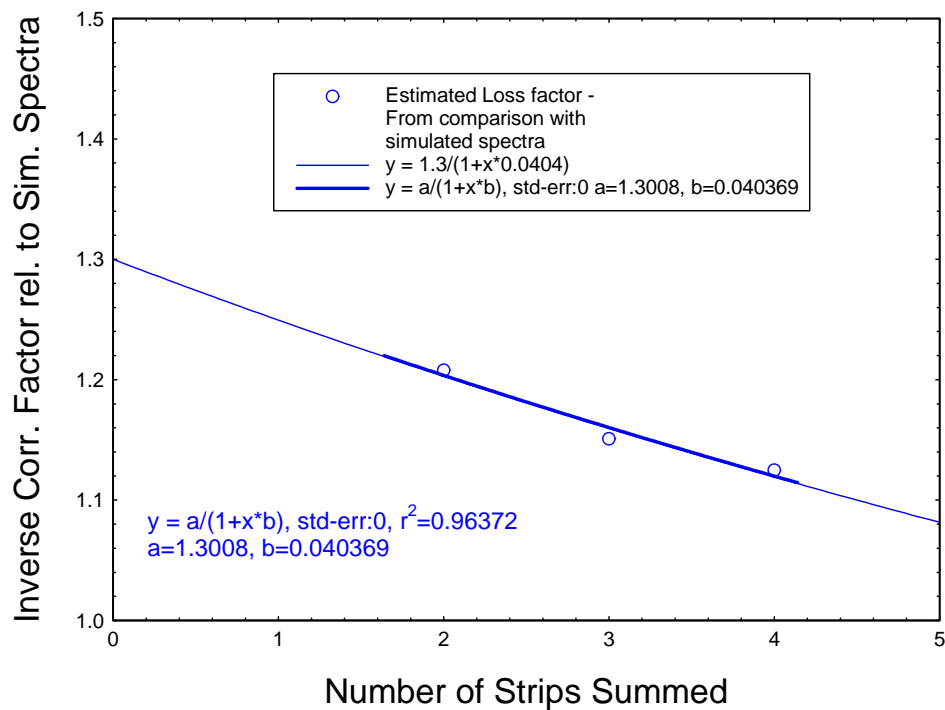


Figure 6: Correction Curve for Capacitive Loading in the PH Spectra.

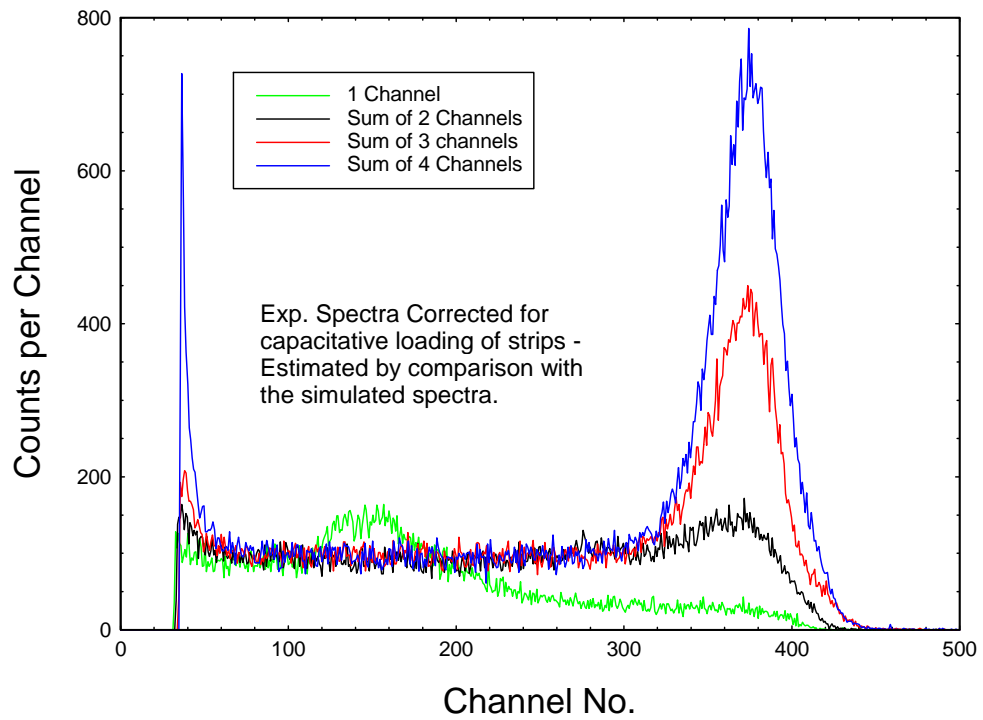


Figure 7: Corrected (Summed) Experimental PH Spectra – using Figure 6.

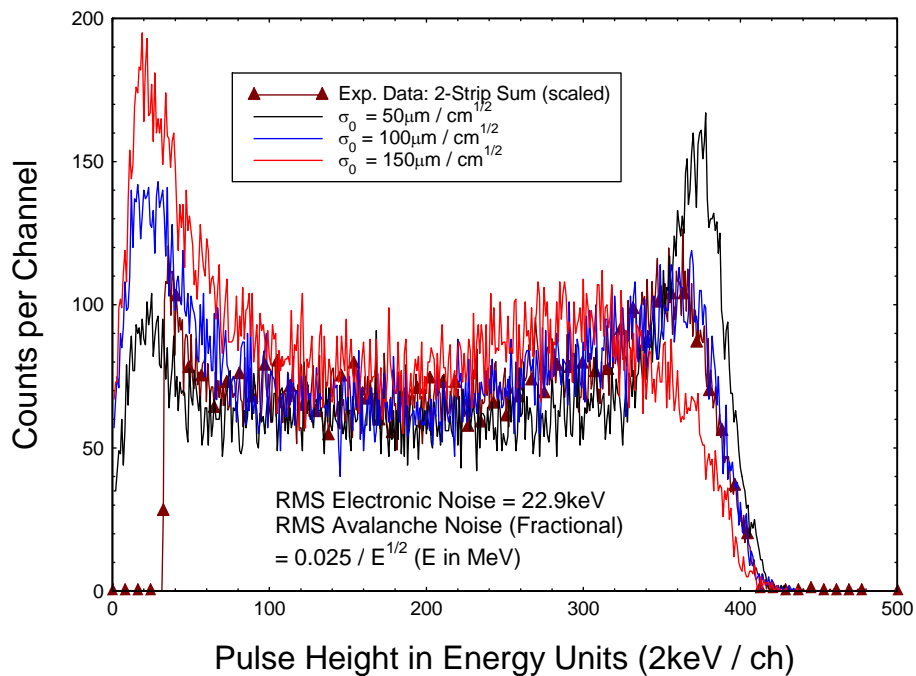


Figure 8: Simulated PH Spectra with varying Electron Diffusion Constants.

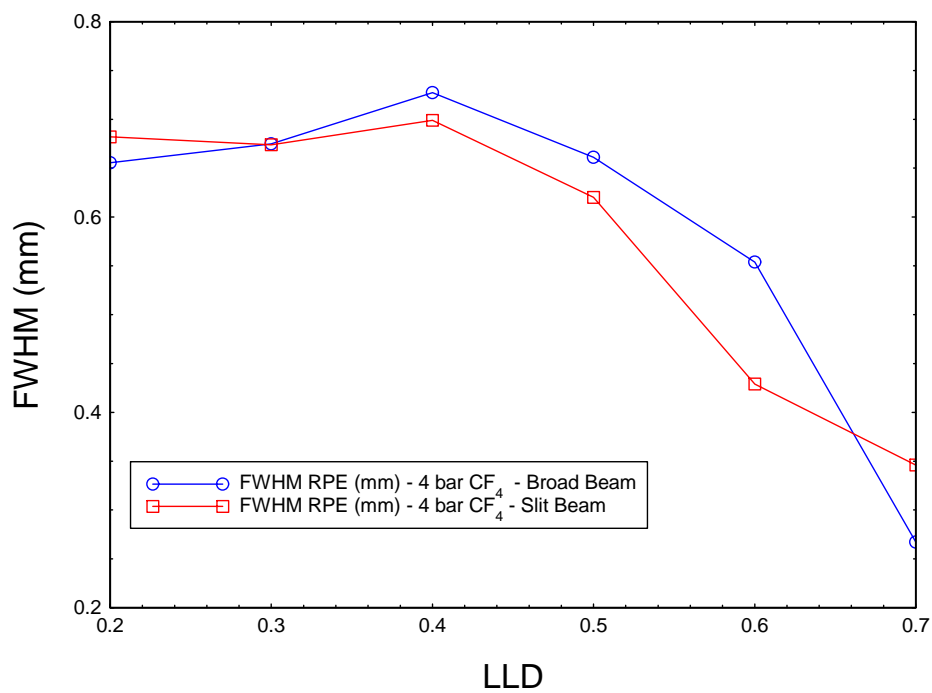


Figure 9: Comparison of Slit and Broad Beam FWHM Evaluations (RPE).

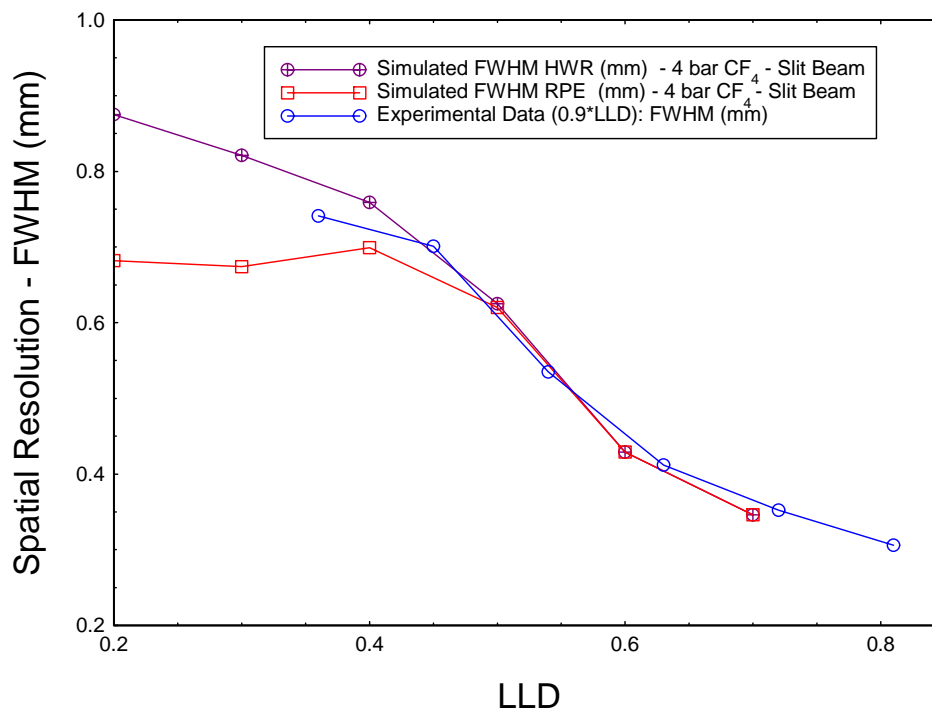


Figure 10: Comparison of Simulated and Observed FWHMs.

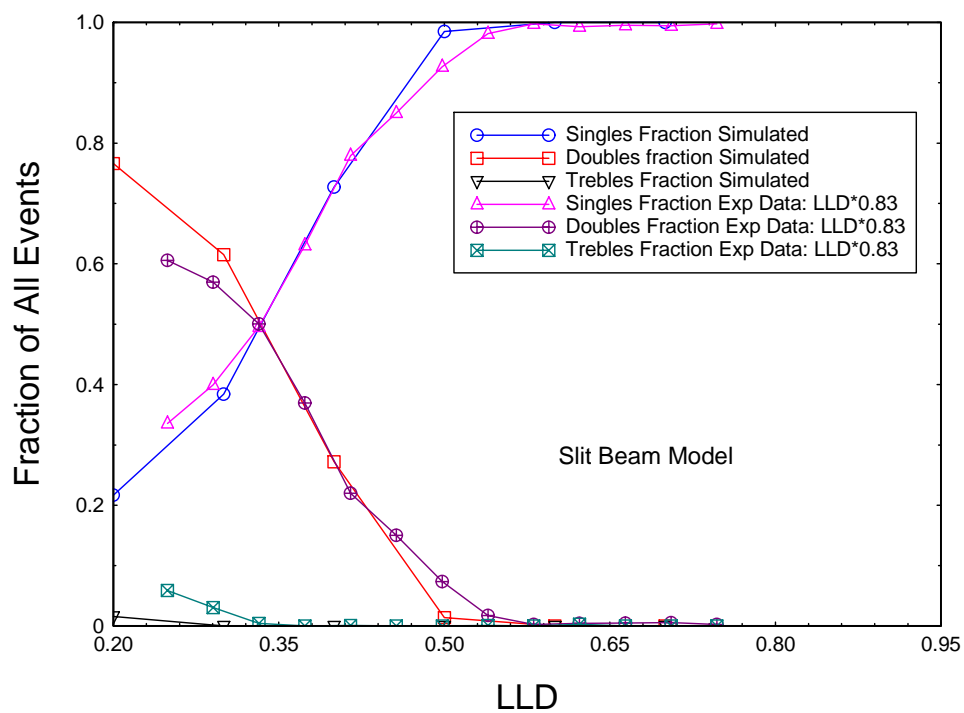


Figure 11: Comparison of the Simulated and Observed Multiplicities.

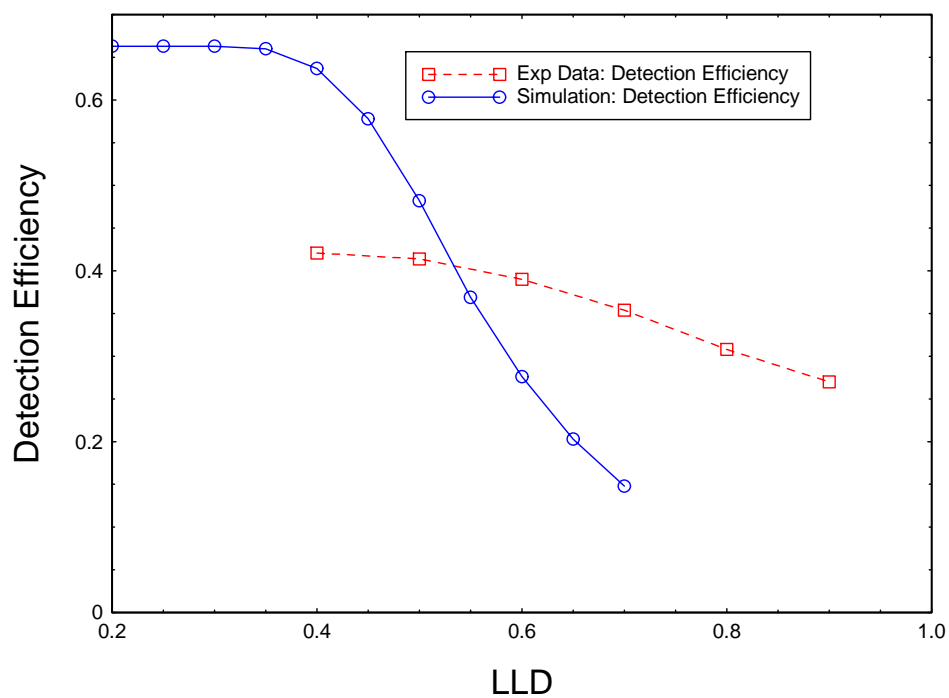


Figure 12: Comparison of the Simulated and Observed Detection Efficiency.

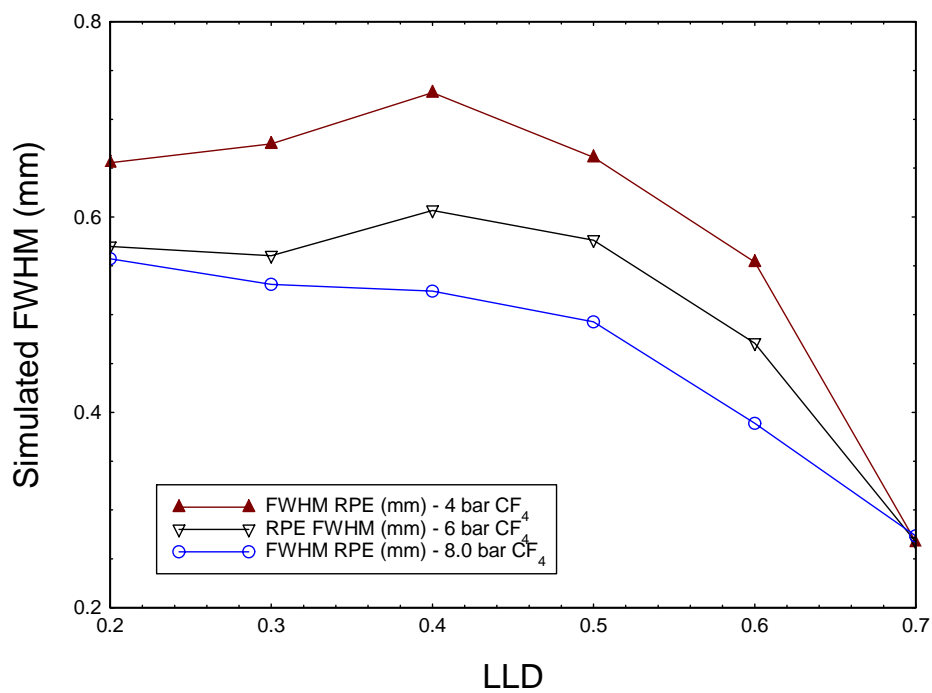


Figure 13: Simulated FWHM (RPE) of OSMOND increasing CF₄ pressure.

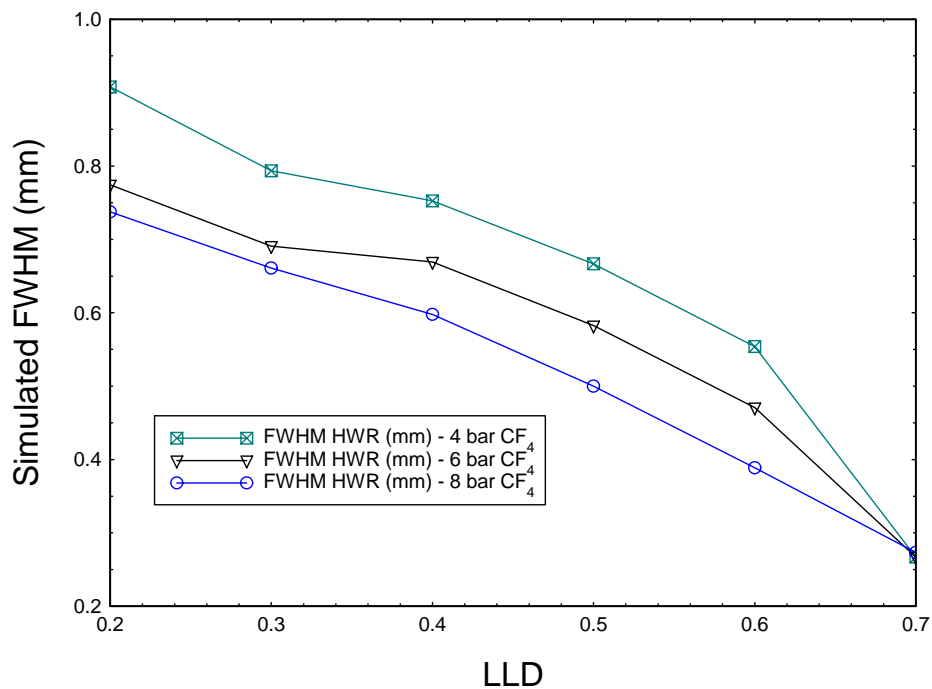


Figure 14: Simulated FWHM (HWR) of OSMOND increasing CF₄ pressure.

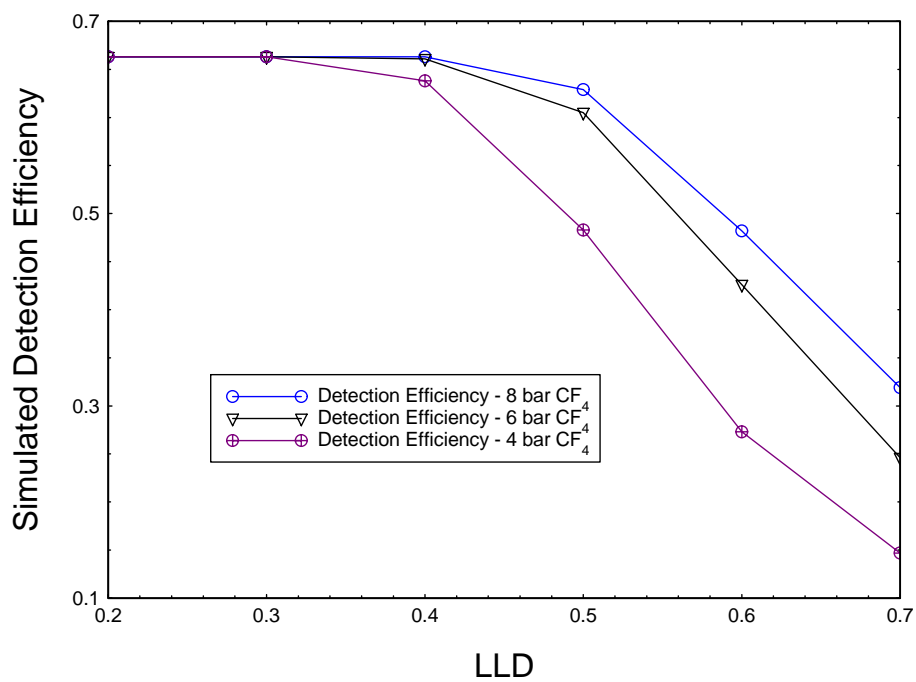


Figure 15: Simulated Detection Efficiency of OSMOND increasing CF₄ pressure.

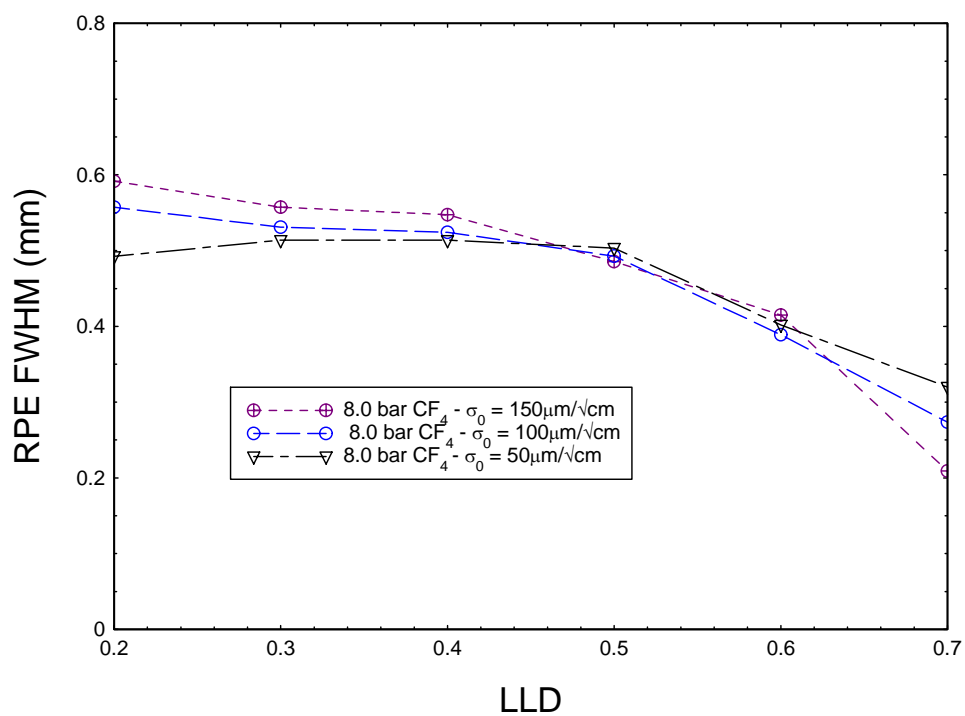


Figure 16: Predicted Sensitivity of FWHM to σ_0 at 8 bar CF₄ Filling.

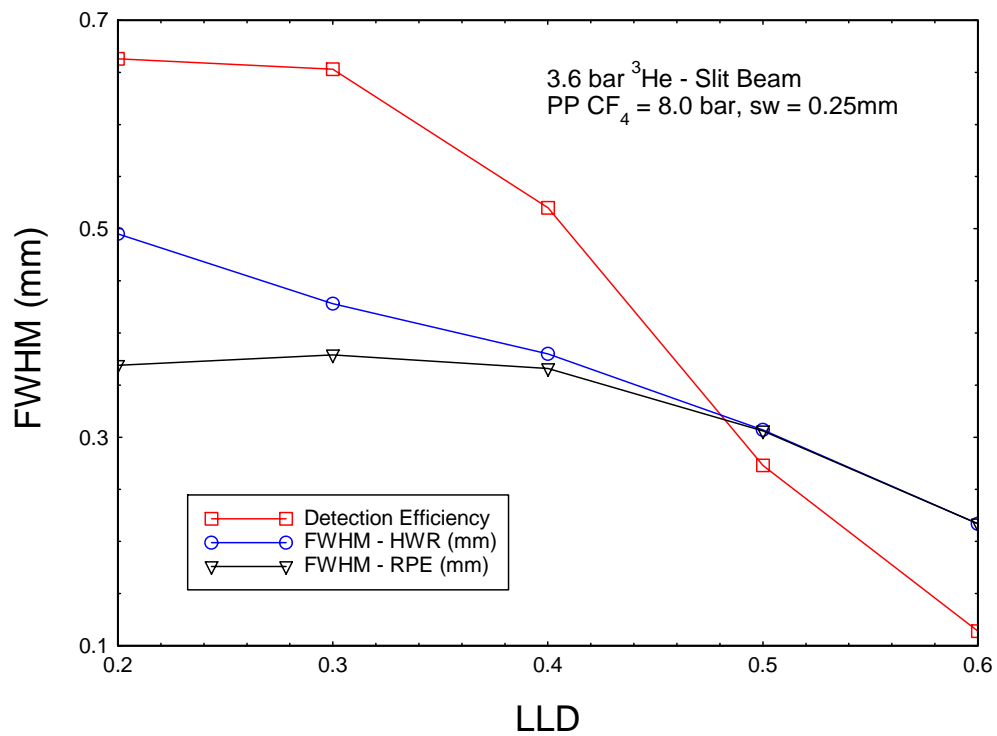


Figure 17: Predicted Performance of OSMOND with Strip Width reduced to 0.25mm and 8 bar CF_4 .